Electrochimica Acta 368 (2021) 137606

Contents lists available at ScienceDirect

Electrochimica Acta

journal homepage: www.elsevier.com/locate/electacta

The effect of naphthalene-based additives on tin electrodeposition on a gold electrode

D. Aranzales[a], I. Briliani[a], I.T. McCrum[a], J.H.O.J. Wijenberg[b], A.C.A. de Vooys[b], M.T.M. Koper[a,*]

[a] Leiden Institute of Chemistry, Leiden University, P.O. Box 9502, Leiden, 2300 RA, The Netherlands
[b] Tata Steel, Research & Development, IJmuiden Technology Centre, P.O. Box 10.000, IJmuiden, 1970 CA, The Netherlands

ARTICLE INFO

Article history:
Received 9 September 2020
Revised 18 November 2020
Accepted 2 December 2020
Available online 5 December 2020

Keywords:
Tin electrodeposition
Gold
Additives
Surface-enhanced Raman spectroscopy

ABSTRACT

In this work, we study the adsorption behavior of naphthalene derivatives: naphthalene (NPT), naphthalenesulfonate (NPTS), hydroxynaphthalenesulfonate (HNPTS) and ethoxylated α-napthalenesulfonic acid (ENSA, a commonly used additive in the tin electroplating industry), on gold electrodes and their effect on the tin electrodeposition process, by means of in situ and ex situ surface analysis techniques (cyclic voltammetry, in situ Surface Enhanced Raman Spectroscopy and ex situ Scanning Electron Microscopy). From experiments and density functional theory calculations, we conclude the formation of films of NPT, NPTS, HNPTS and ENSA, where NPT and NPTS lie flat on the gold surface and HNPTS and ENSA undergo oxidative polymerization. The nature and stability of the films are strongly dependent on the surface structure, interaction between the molecules, and applied potential. NPTS is observed to form a denser film than NPT due to attractive interactions between the adsorbed molecules on gold and tin. Tin electrodeposition is strongly affected by the presence of the NPT, NPTS, HNPTS and ENSA films. Tin bulk electrodeposition is inhibited in the presence of NPT and NPTS, but slightly promoted in the presence of HNPTS. Tin deposits grown in the presence of NPT and NTPS have the same morphology, and the characteristic size of the electrodeposited features is smaller than in their absence. The tin deposit grown in the presence of HNPTS exhibits markedly different and smaller features. Some amount of sulfur form is incorporated in the deposit as a result of the reductive desulphonation of NPTS, HNPTS and ENSA on the gold electrode. The effect of ENSA was compared to the results obtained with NPT, NPTS and HNPTS. ENSA exhibits a similar behavior to NPT, NPTS and HNPTS during tin deposition process in terms of the voltammetry of tin deposition, but it severely inhibits the bulk deposition. Naphthalene derivatives and ENSA have an effect on the tin bulk deposition process, but show no or little effect on the formation of AuSn (surface) alloys, which is ascribed to the slow nature of Sn UPD on gold and the SnAu alloying process.

1. Introduction

Most of the plating solutions used in the electrodeposition of metals and alloys contain at least one inorganic or organic additive [1]. Additives play an important role in metal plating, such as reduction of substrate roughness, reduction of the grain size of the deposit, production of specific micro- and macro-structures, increase of the corrosion resistance, among others. Numerous studies have been performed in order to understand the role of the additives during metal deposition [2,3]. The effect of additives has been the most extensively studied for copper electrodeposition [4–11], for instance by showing their strong influence on the surface structure of the substrate, the lifting of the reconstruction as a consequence of additive adsorption [4,12], or the creation of surface vacancy islands [6]. Changes during the nucleation and growth are also common when organic molecules are added, such as an increase in the number of nuclei [7] and the decrease in the kinetics of electrodeposition [5].

Tin electrodeposition is a common electroplating process used in multiple applications: corrosion protection, electronics fabrication, packaging industry, and many others. During the past 20 years, developments in tin plating have allowed the extension of its applications to batteries and semiconductor industry [13]. High-

* Corresponding author.
E-mail address: m.koper@chem.leidenuniv.nl (M.T.M. Koper).

https://doi.org/10.1016/j.electacta.2020.137606

quality tin coating baths require the addition of different compounds, especially organics, in order to have the desired chemical and physical properties of the deposit. Aromatic compounds are broadly used in tin electrodeposition, but the chemical structure of the common additives is quite diverse and complex, which makes understanding their exact effect difficult.

Previous work on the effect of aromatic carbonyls [14–16] has ascribed differences in the grain size and crystalline orientation of the tin deposits to the strong adsorption of the additives or their reduction products [15] onto the metal substrate, where additives block active sites and promote preferential tin growth. Martyak et al. studied glycol-type additives [17] and ascribed the increase of the tin (II) reduction overpotential to changes in the kinetics of the process. Barry et al. studied phenyl-2-butenalimine and formaldehyde and ascribed the same effect to changes in the nucleation and growth mechanism [18]. Studies of much more complex molecules such as the commonly used ethoxylated α-napthalenesulfonic acid (ENSA) have shown that it enhances the quality of tin deposits, which was ascribed to kinetic and mass transport limitations due to the formation of ENSA aggregates on the electrode [19,20].

In this work we study the effect of naphthalene derivatives: naphthalene (NPT), naphthalenesulfonate (NPTS), hydroxynaphthalenesulfonate (HNPTS) and ethoxylated α-napthalenesulfonic acid (ENSA), on tin electrodeposition on a gold electrode. Gold was chosen as a substrate due to its wide double layer window and weak chemisorbing properties. The electrochemistry of (single-crystal) gold has been well studied [12]. These properties facilitate the understanding of molecular adsorption and metal deposition studies. We use the results obtained with NPT, NPTS and HNPTS (with simple chemical structures) as a model to obtain insights into the effect of a much more complex chemical structure, such as ENSA, a commonly used additive in industrial tin plating. Naphthalene derivatives and tin electrodeposition are studied by conventional electrochemical techniques as well as by means of in situ SERS (surface enhanced Raman spectroscopy), ex-situ SEM (scanning electron microscopy) and density functional theory calculations.

2. Experimental and computational details

2.1. Experimental details

All glassware was stored overnight in a solution of 1 g L^{-1} $KMnO_4$ in 0.5 M H_2SO_4. Before use, it was rinsed with water and 30% hydrogen peroxide solution in order to remove permanganate anions and trace impurities. Glassware was boiled in water five times before starting the experiments. The water used to clean glassware and to prepare solutions was demineralized and ultra-filtrated by a Millipore MilliQ system (18.2 MΩ cm). A gold wire was used as a counter electrode and a reversible hydrogen electrode (RHE) was used as a reference, but all the potentials were converted to the normal hydrogen electrode (NHE), by using the following equation: $E_{RHE} = E_{NHE} - 0.0591\,pH$. The reference electrode was in contact with the electrolyte via a Luggin capillary. A capacitor of 10 µF was connected to an additional gold wire in solution and the RHE electrode to filter small currents produced in the RHE electrode and reduce the noise in measurements at low currents. The working electrode was either a gold single crystal disk electrode (diameter 7 mm, 1 mm thick), used in the hanging meniscus configuration, or a polycrystalline gold disk electrode (5 mm diameter, 4 mm thick) used in the rotating-disk electrode (RDE) setup under hydrodynamic conditions. Cyclic voltammetry experiments were performed using a potentiostat PGSTAT 12 (Metrohm-Autolab). RDE experiments were performed with an MSR rotating electrode (Pine Research) at a rotation rate of 1600 rpm. The electrode potential was corrected for Ohmic drop during the measurements, by using 85% of the Ohmic resistance measured by electrochemical impedance spectroscopy.

Single crystal gold electrodes were cleaned before each experiment by flame annealing for about 5 s, and subsequently cooled in air and quenched in deionized water; the procedure was repeated 10 times. To check the quality of the surface and cleanliness of the solution (0.1 M H_2SO_4) a cyclic voltammogram was taken at potentials between 0.06 to 1.26 V at 50 mV s^{-1}. In the case of the polycrystalline gold surface, the electrode was cleaned electrochemically: first by oxidizing it in 0.1 M sulfuric acid by applying 10 V for 20 s, using a graphite bar as a counter electrode, after which the gold oxide formed was removed by dipping the working electrode in a 6 M HCl solution for 30 s. Subsequently, the polycrystalline gold electrode was mechanically polished by using diamond powder suspension (0.05 µm particle size) during 5 min, rinsed and transferred to an ultrasound bath with water. Finally, the electrode was electropolished in a 0.1 M H_2SO_4 solution by 200 cycles between 0.06 to 1.81 V at 1 V s^{-1}. Additionally, before every measurement, a cyclic voltammogram of the gold surface was recorded at potentials between 0.06 to 1.81 V at 50 mV s^{-1}. Scanning electron micrographs of the bare polycrystalline gold and gold single crystals surfaces prior to the experiments are presented in the Fig. S17.

In situ Surface Enhanced Raman Spectroscopy (SERS) measurements were performed with a confocal Raman microscope (LabRam HR, Horiba Yobin Yvon) with a 50x objective. A He/Ne laser of 633 nm was used as the excitation source. Reference and counter electrodes were the RHE and a gold wire, respectively. The working electrode was a roughened gold disk electrode of 4 mm diameter. The gold electrode was roughened as follows: The electrode was cleaned via mechanical polishing, electrochemical etching and electropolishing (see previous paragraph). Once the surface was clean, it was transferred to a separate cell containing 0.5 M KCl, and 50 cycles of step potentials were applied: 0.3 V during 15 s and 1.2 V during 5 s. Afterwards, the electrode was rinsed and transferred to the Raman cell to perform the in-situ spectroscopic measurements. A spectrum at 1.06 V was taken in the electrolyte without the presence of NPTS as a baseline.

The morphology of the metal deposits was observed by a scanning electron microscopy SEM. Micrographs were taken using the model JEOL 820 SEM at 15 kV. Energy Dispersive X-Ray Spectroscopy (EDS) measurements were taken at 15 kV, the reported percentage of tin was calculated from the average of relative ratio of tin from a line scan measurement of 0.5 µm length, over the tin features.

All solutions were prepared from chemicals with the highest purity commercially available: H_2SO_4 (96% ultrapure, Merck), $SnSO_4$ (≥95%, Sigma Aldrich), naphthalene (≥99%, Sigma Aldrich), 2-napthalenesulfonic acid sodium salt (99.6%, Sigma Aldrich), sodium thiosulfate (≥99.99%, Sigma Aldrich), 4–hydroxy-1-naphthalenesulfonic acid sodium salt (≥95%, Santa Cruz Biotechnology) and ethoxylated α-napthalenesulfonic acid (73.6%, Pulcra chemicals). In the case of ENSA the main impurities are sulfuric acid with 8.7%, and water with 2.4%, other impurities were not provided by the supplier.

A low Sn^{2+} concentration (0.6 mM), an oxygen-free atmosphere (permanent argon bubbling), and a pH lower than 2, were chosen in order to avoid the contribution of polymeric Sn (II) species and hydrolysis products formed in the bulk of the solution [21–24].

The number of deposited tin monolayers (ML) was calculated from the charge that flowed during the experiment, taking as reference the accepted value of the charge of a monolayer on polycrystalline gold surface: 390 ± 10 µC cm^{-2} [25]. The total charge of the deposit is the addition of the cathodic charge calculated from the area under the linear sweep voltammetry curve, between 0.659 to −0.241 V and the charge calculated from the product between

the current at −0.241 V and the time that the potential was held (60 s) at it. The corresponding electrochemical experiments are shown in Figure S16 in the Supporting Information. We assumed that the only reaction taking place in this range of potential is tin electrodeposition.

2.2. Computational details

The lateral interaction energy between naphthalene and naphthalenesulfonic acid on Au (111) and Sn (111) was calculated using density functional theory (DFT). DFT simulations were performed using the Vienna Ab-initio Simulations Package (VASP) [26–28]. A plane wave basis set was used with a cutoff energy of 450 eV. Ion core potentials were modeled using the Projector Augmented Wave (PAW) approach [29,30] and the PBE exchange-correlation functional [31,32] was used. Structural optimizations were carried out until the forces on each atom were below 0.02 eV $Å^{-1}$. Dipole corrections were applied in the surface normal direction [32]. The unreconstructed Au(111) surface was modeled in a 4 × 8 unit cell with a 5 × 3 × 1 Monkhorst-Pack [32] k-space sampling grid. The surface was comprised of four atomic layers with the bottom two layers frozen at the experimentally measured lattice constant of 4.08 Å [33]. The unreconstructed Sn(111) surface was modeled in a 3 × 6 unit cell with a 5 × 5 × 1 k-space grid, and was comprised of 8 atomic layers with the bottom two layers frozen at a lattice constant of 4.7 Å (for α–Sn) [34]. Van der Waals interactions are approximated using the DFT-D3 method [35,36]. Binding energies of naphthalene and naphthalenesulfonic acid are calculated for adsorption on Au (111) both without and with the van der Waals correction (all calculations of the lateral interaction energy include the correction).

To approximate the lateral interaction energy, both naphthalene and naphthalenesulfonic acid were first modeled on Au(111) in a (4 × 4) structure, as found experimentally by Wan et al. for naphthalene on Cu(111) [37], in a 4 × 8 unit cell, containing two naphthalene or naphthalenesulfonic acid molecules. The change in energy (0 K DFT energy, neglecting entropy and vibrational energy) was then calculated for a similar structure but with the two molecules in the 4 × 8 unit cell brought closer together. This interaction was found to be attractive for both naphthalene and naphthalene sulfonic acid, however, the magnitude was very small (−0.02 eV) for naphthalene. A configuration where the sulfonate groups could hydrogen bond between the two naphthalene sulfonate molecules was also examined. In this case, one of the two naphthalene sulfonic acid molecules were rotated, so that the sulfonate groups were in close proximity. The hydrogen bonded configuration was found to be more stable. A similar procedure was used to study the lateral interactions on Sn (111), though an experimentally measured ad-layer structure on this surface could not be found in prior literature; a similar structure as that found on Au (111) was used.

While only a small number of configurations were examined, the configurations examined for both naphthalene and naphthalenesulfonic acid were identical; the interactions were significantly

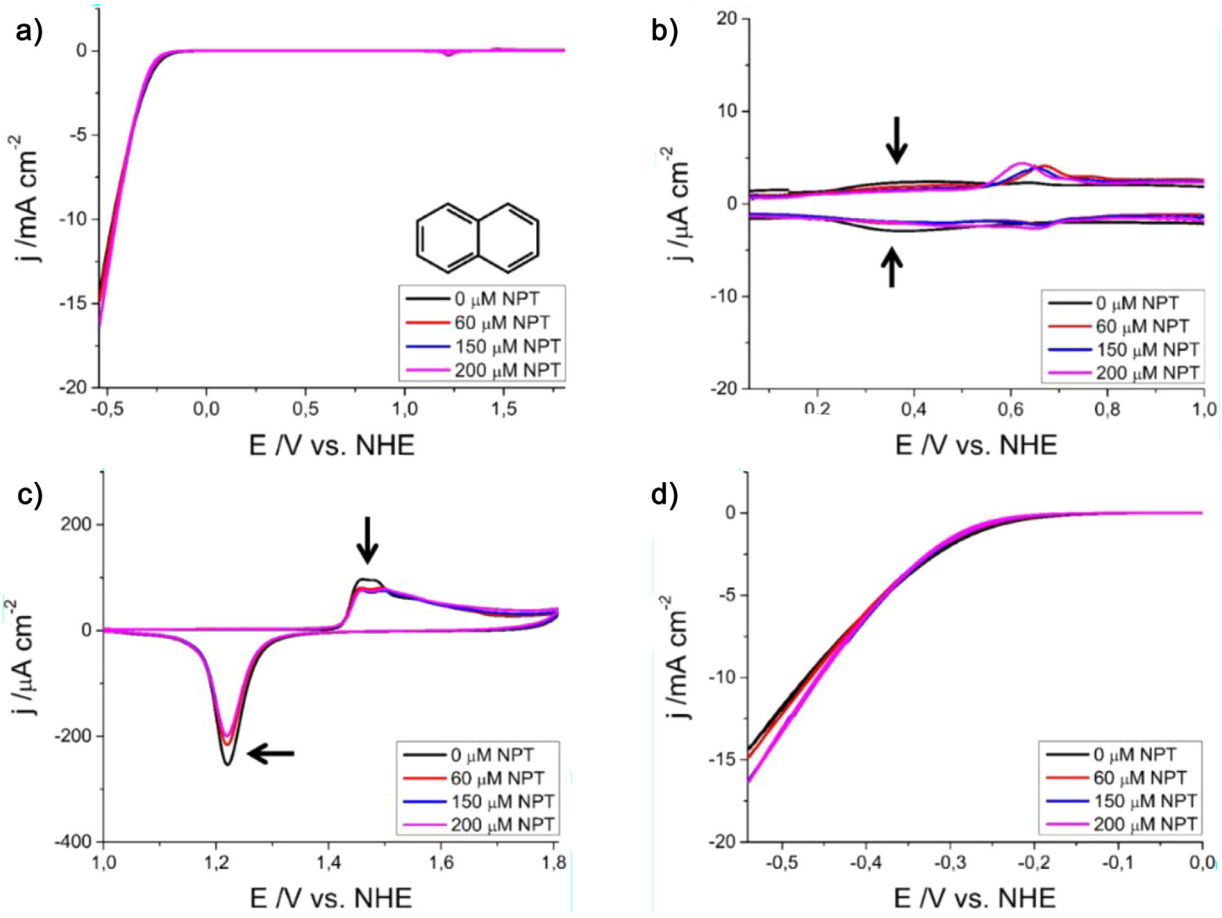

Fig. 1. Cyclic voltammograms of a polycrystalline gold disk electrode in 0.1 M H_2SO_4 at different NPT concentrations (a) CV recorded between −0.54 to 1.81 V at 50 mV s^{-1}. (b) Zoom-in of the double layer region, arrows show the decrease in the capacitive current (c) Zoom-in of the gold oxide formation and reduction region, arrows show the decrease in the peak currents (d) zoom-in of hydrogen evolution region (HER). (For interpretation of the references to color in this figure legend, the reader is referred to the web version of this article.)

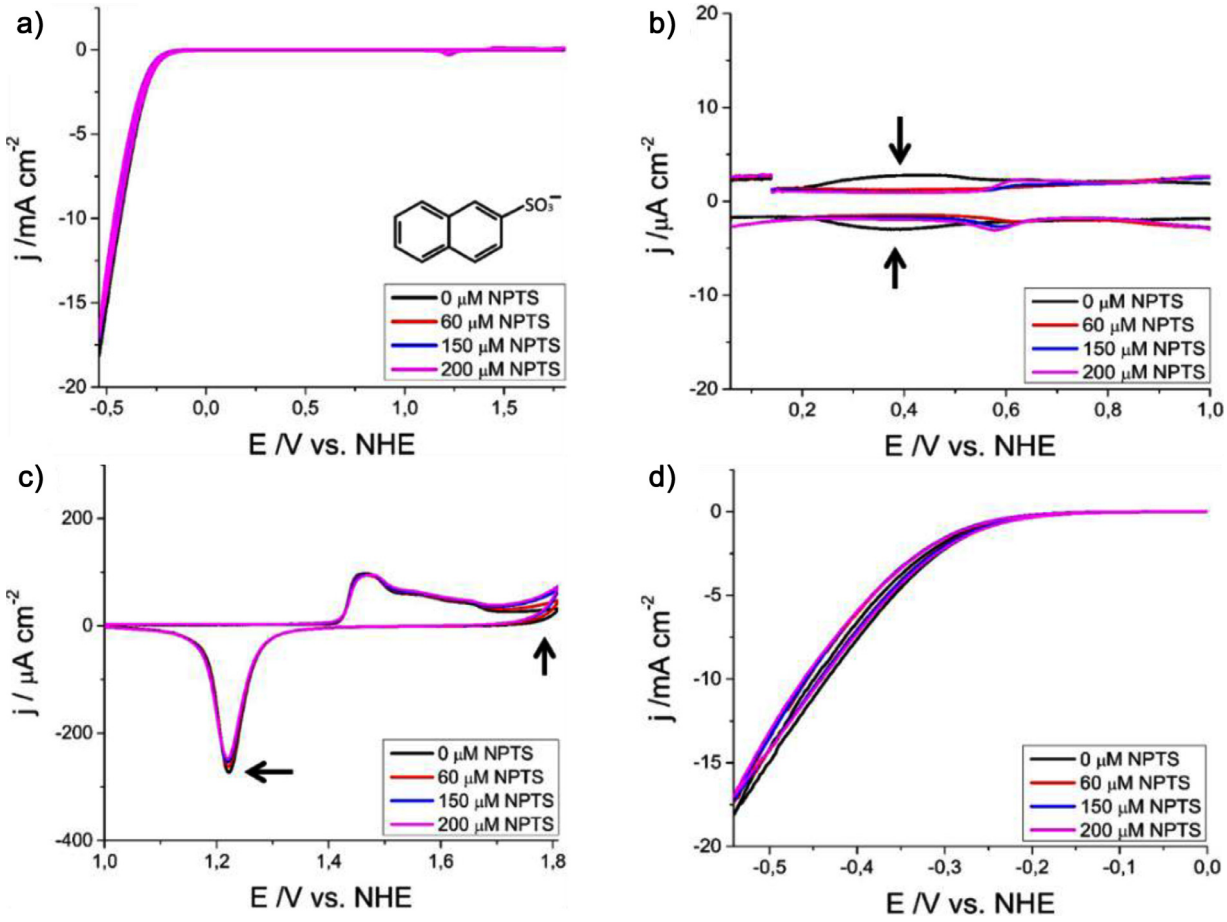

Fig. 2. Cyclic voltammograms of a polycrystalline gold disk electrode in 0.1 M H_2SO_4 at different NPTS concentrations (a) CV recorded between −0.54 to 1.81 V at 50 mV s^{-1}. (b) Zoom-in of the double layer region, arrows show the decrease in the capacitive currents (c) Zoom-in of the gold oxide formation and reduction region, arrows show the decrease in the reduction area and the emergence of oxidative currents at very positive potentials (d) zoom-in of hydrogen evolution region (HER). (For interpretation of the references to color in this figure legend, the reader is referred to the web version of this article.)

more attractive for the naphthalenesulfonic acid than for the naphthalene. This interaction energy does not include the effect of the presence of solvent near the electrode surface (which could affect, for example, the energy gained on pairing/hydrogen-bonding neighboring naphthalenesulfonic acid molecules).

3. Results and discussions

Cyclic voltammetry measurements of polycrystalline gold in a wide potential window (−0.54 to 1.81 V) in the presence of naphthalene (NPT) and naphthalenesulfonate (NPTS) at different concentrations are shown in Figs. 1 and 2, respectively. The measurements show that neither NPT or NPTS strongly modify the CV profile of the gold surface, in the sense that the onset potential and current profile for the gold (hydr-)oxide formation is not affected significantly (Figs. 1a and 2a), and the activity for the hydrogen evolution reaction (HER) is also not strongly affected. However, Figs. 1 and 2 show new features in the double layer region between 0.58–0.62 V, which are dependent on the NPT and NPTS concentration. Simultaneously, a decrease in the current density and capacity in the double layer region between 0.2 and 0.5 V are also observed.

Although Figs. 1 and 2 show only minor effects on the gold hydr(oxide) formation and reduction at positive potentials and the HER activity at negative potentials, both NPT and NPTS lead to changes in the current density in the double layer region, which may be explained by the formation of a film [38,39]. It is known that organic molecules can be adsorbed at the metal surface by organizing spontaneously into monolayers. The formation of such films typically manifests in a characteristic decrease of the double layer capacity [5,39].

Fig. 3 shows cyclic voltammetry measurements of polycrystalline gold in a wide potential window (−0.54 to 1.81 V) in the presence of hydroxynaphthalenesulfonate (HNPTS) at different concentrations. The cyclic voltammogram exhibits some distinct features in comparison to NPT and NPTS. The double layer region presents at least three different peaks (A – C) that do not appear in the voltammetry of NPT and NPTS. These peaks exhibit a linear relationship between peak current and the scan rate, indicating that they involve adsorbed species. Above 1.1 V, there are two anodic peaks (D and E) that are not related to adsorption processes, as they do not have a reductive counterpart; instead they seem associated to the oxidation of HNPTS, likely involving oxidative polymerization of the naphthol, leading to the formation of a polymer film [40–43]. The presence of this polymer film is confirmed by the considerably higher capacitance measured in the presence of HNPTS, suggestive of a thicker film that can store ions. Finally, hydrogen evolution is slightly hindered as a consequence of HNPTS adsorption, at least more than in the presence of NPT and NPTS.

In Fig. 4, we show the cyclic voltammetry of a polycrystalline gold electrode in the presence of different concentrations of ENSA. The CVs are qualitatively more similar to the voltammetry in the presence of HNPTS than to the voltammetry in the presence of NTP and NTPS: there are new peaks in the voltammetry between 0.6

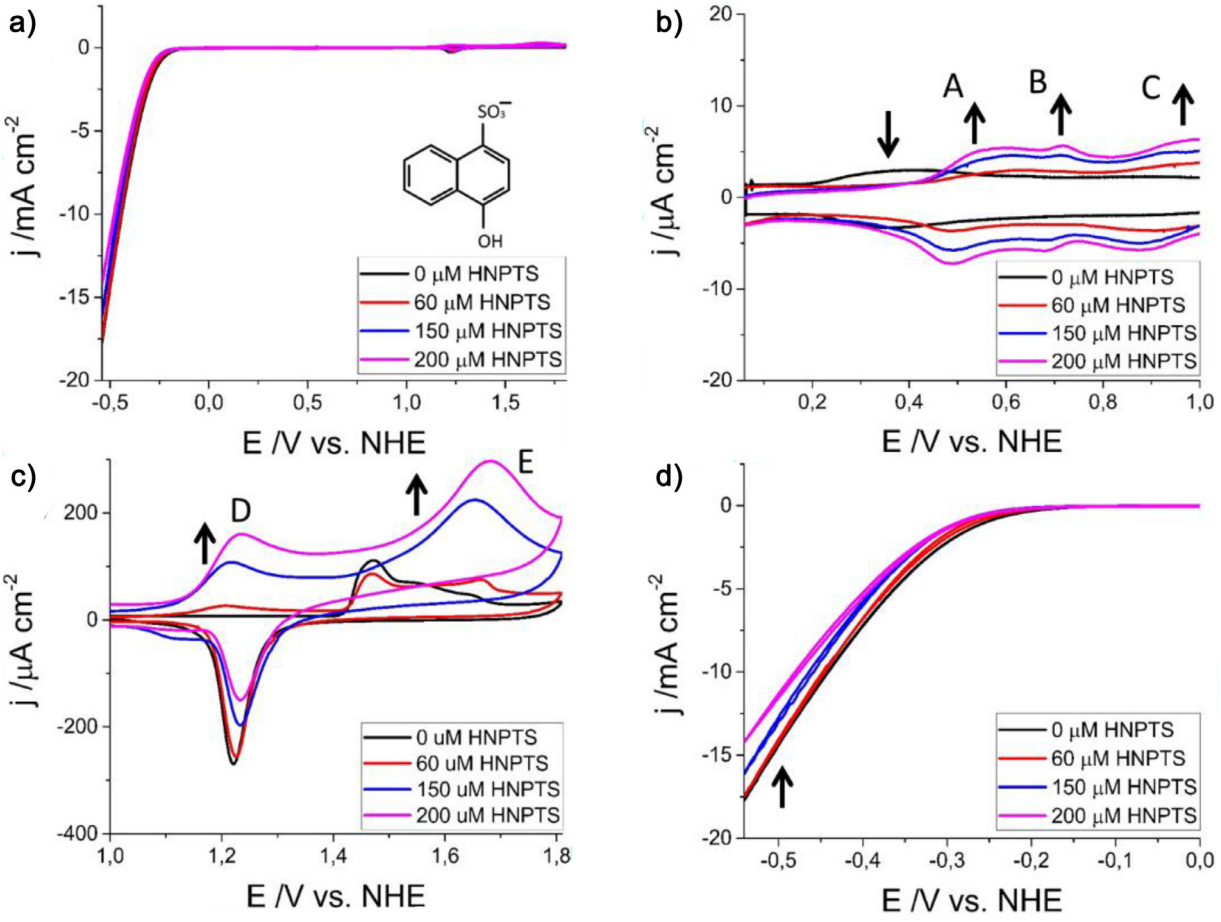

Fig. 3. Cyclic voltammograms of a polycrystalline gold disk electrode in 0.1 M H_2SO_4 at different HNPTS concentrations (a) CV recorded between −0.54 to 1.81 V at 50 mV s^{-1}. (b) Zoom-in of the double layer region, arrows show the decrease in the capacitive currents and the rise of at least three anodic peaks (c) Zoom-in of the gold oxide formation and reduction region, arrows show the emergence of two anodic peaks (d) zoom-in of hydrogen evolution region (HER), arrow shows a slight decrease in the cathodic current. (For interpretation of the references to color in this figure legend, the reader is referred to the web version of this article.)

and 1.0 V (Fig. 4b), which relate to surface adsorbed states, and there is an oxidation current above 1.1 V which does not have a reductive counterpart (Fig. 4c). Together with the high double-layer capacitance (Fig. 4b), this strongly suggests the formation of a polymer film formed oxidatively. Also, ENSA has a rather strong inhibitive effect on the hydrogen evolution (Fig. 4d).

Since the nature and stability of electro-adsorbed organic films are strongly dependent on the crystalline surface structure, experiments on single-crystal Au surfaces were performed. Figs. 5a-d show the cyclic voltammetry of Au (100) at different concentrations of NPT, NPTS, HNPTS and ENSA, respectively. We show here only results on Au (100), as the effects on this surface are the strongest, specifically on the surface reconstruction; results on Au (111) and Au (110) are shown in the Supporting Information (see Fig. S1- S3, S5-S7).

The effect of NPT on Au (100) (Fig. 5a) is primarily on the peak at 0.68 V, ascribed to the lifting of the (hex) reconstruction on Au(100) [12], which presents a decrease in its intensity, and a shift towards less positive potentials with an increase of NPT concentration. Since it is well known that on Au(100), the lifting of the reconstruction is related to anion adsorption [12], it appears that the presence of naphthalene molecules on the gold surface hinders sulfate adsorption. The presence of NPT on gold leads to a slightly lower double-layer capacity giving rise to a decrease of the current density between 0.16 – 0.66 V. The naphthalene adlayer appears to be more energetically stable on the unreconstructed Au (100) -(1 × 1) surface, and therefore the reconstruction is lifted at less positive potentials. The potential window labeled 3 in Fig. 5a shows a reversible peak at ca. 0.81 V. This peak corresponds to sulfate adsorption, as it is absent in perchloric acid (see Fig. S4 in the Supporting Information). In the absence of NPT, the peak at 0.68 V corresponds to a sulfate phase transition occurring concomitantly with lifting of the (hex) reconstruction [44]. The presence of NPT on the surface hinders the sulfate adsorption, shifting it to more positive potentials. In the potential window labeled 4, the Au (100) surface still shows a lower capacitive current density, which indicates the wide adsorption range of naphthalene molecules on the Au (100) surface. We conclude that naphthalene molecules are adsorbed on the gold surface over a wide potential window, essentially the entire double layer window, blocking sulfate anions from access to the surface.

The adsorption of NPTS exhibits a somewhat different behavior, as illustrated in Fig. 5b. Two reversible couples are seen in the potential windows labeled 1 and 3, around 0.11 and 1.04 V, respectively. Most importantly, Fig. 5b does not show the peak around 0.68 V, assigned to the lifting of the reconstruction on the Au (100) by the anion adsorption [12]. Also, the peak at 0.81 V that is observed in the presence of NPT, is missing in the presence of NPTS. Compared to the CV in the presence of NPT, this suggests that a more compact film is formed in the presence of NPTS, blocking the sulfate adsorption on the Au (100) surface better than NPT.

Fig. 5c shows new features compared to the voltammetry with NPT and NPTS, largely in agreement with what is observed for polycrystalline gold: oxidative current without reductive counter-

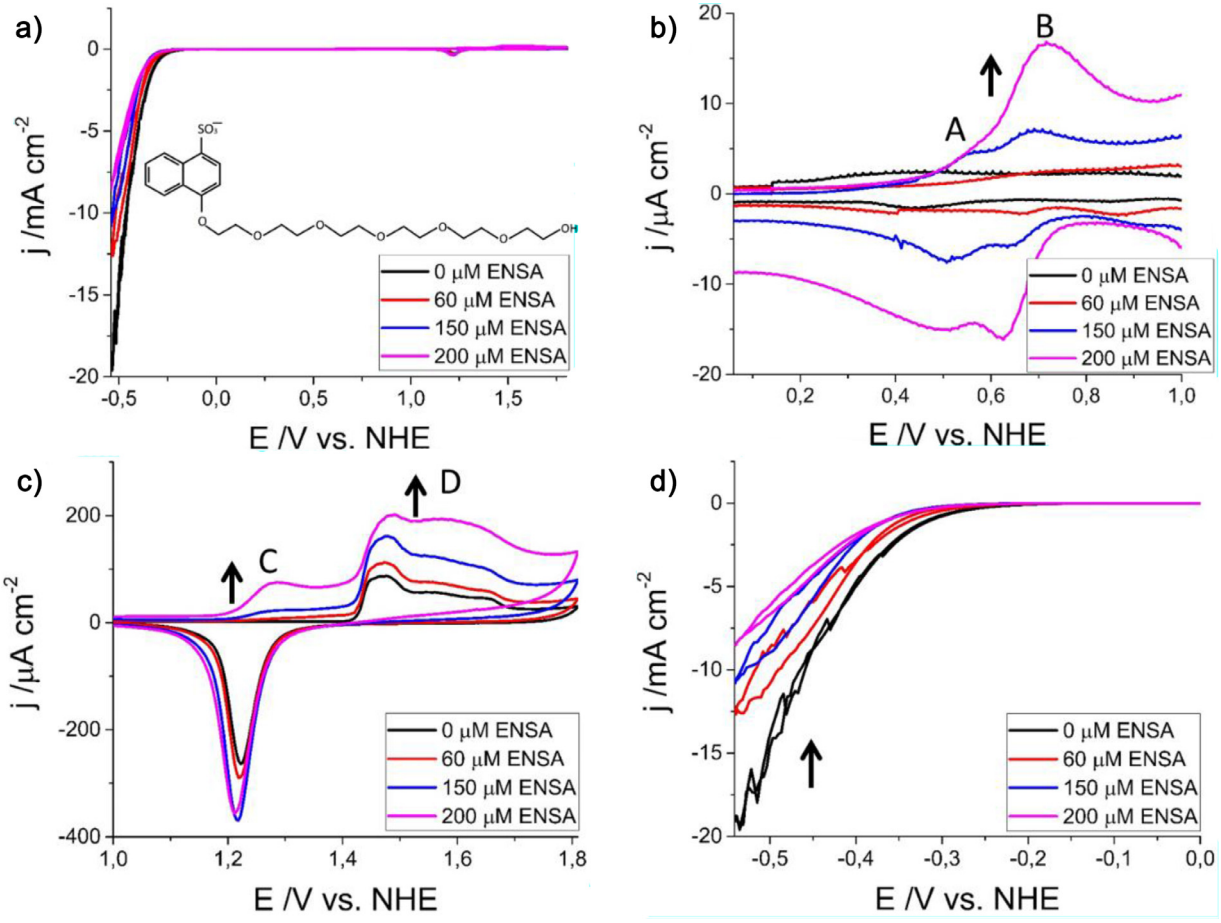

Fig. 4. Cyclic voltammograms of a polycrystalline gold disk electrode in 0.1 M H_2SO_4 at different ENSA concentrations (a) CV recorded between −0.54 to 1.81 V at 50 mV s^{-1}. (b) Zoom-in of the double layer region, arrow show the increase of a peak with the increasing ENSA concentration (c) Zoom-in of the gold oxide formation and reduction region, arrows show the emergence of oxidative currents at positive potentials (d) zoom-in of hydrogen evolution region (HER), arrow shows the strong decrease of HER. (For interpretation of the references to color in this figure legend, the reader is referred to the web version of this article.)

part, and a higher double-layer capacity. As mentioned, previous studies have shown polymerization of naphthol as a consequence of oxidation under acidic conditions [40–43] which we suspect also happens with HNPTS. Fig. 5d shows the effect of ENSA on the voltammetry of Au (100), which is again very different from Fig. 5a and 5b, but qualitatively similar to Fig. 5c: irreversible oxidation at high potential, and higher double-layer capacity.

Surface Enhanced Raman Spectroscopy (SERS) was used to obtain more information about NPT, NPTS, HNPTS and ENSA adsorption. Fig. 6 shows that NPT gives rise to a very low intensity band at ~1374 cm^{-1} between 0.56 to 0.96 V, the band is ascribed to the characteristic C–C stretching of NPT ring planar oriented on Au. This observation is in agreement with previous studies of Busby and Creighton that showed the same band at 1376 cm^{-1}, and ascribed it to naphthalene ring mode on a planar orientation on Au and Ag electrodes [45]. Dahms and Green also showed evidence for the planar position of naphthalene on the gold surface by means of the shape of the adsorption isotherm using a ^{14}C-radio tracer technique [46], and Wan and Itaya demonstrated by electrochemical scanning tunneling microscopy (STM) that naphthalene molecules are flat oriented on the copper surface [47].

Fig. 7 shows the evolution of SER spectrum of NPTS on gold recorded in a potential window from 0.01 to 1.06 V. Similar to NPT, the NPTS spectrum exhibits a band at ~1370 cm^{-1} ascribed to C–C stretching of the NPT ring flat oriented on the Au surface. Interestingly, the SER spectra show that between 0.26 to 0.56 V a second band appears at ~1430 cm^{-1} which is ascribed to symmetric stretching of ν_s (C–C) [48–51] of the naphthalene ring, coinciding with the region of the lowest differential capacity in Fig. 2b. Based on these observations, in combination with the DFT calculations, we propose that a flat orientation is the most likely adsorption mode of NPT and NPTS.

Fig. 8a shows the evolution of SER spectrum of HNPTS on gold between 0.01 to 0.46 V. The spectra at 0.01 and 0.06 V exhibit a considerable number of bands presumably ascribed to vibrational modes of the naphthalene ring, sulfonate and hydroxyl groups. We ascribed bands at 1460, 1502 and ~1560 cm^{-1} to vibrational modes of the naphthalene ring such as symmetric stretching of ν_s (C–C) and in plane bending of β(H–C-C) [48–51]. Bands at 540 cm^{-1} to scissoring of δ (-SO_2-) [48], at 1363 cm^{-1} to antisymmetric stretching ν_{as} (-SO_2-) [48,49], and 2112 cm^{-1} to stretching of ν(OH) from (C-SO_3^- H_3O^+) [49] of the sulfonate group. Additionally, the band at 1300 cm^{-1} is ascribed to in plane bending [β(H–O)] [52] of OH group bound to the naphthalene ring. Between 0.16 and 0.46 V, the SER spectra exhibit remarkable changes; it roughly coincides with the adsorption peaks A and B in the voltammogram of Fig. 5c (see also Fig. S5c). From 0.46 to 0.86 V (see Fig 8b), the spectra mainly show two peaks, one at 1394 cm^{-1} ascribed to antisymmetric stretching ν_{as} (-SO_2-) [48,49] of the sulfonate group and the other one at 1579 cm^{-1} ascribed to symmetric stretching ν_s (C–C) [48] and in-plane bending β(H–C-C) [48–51] of the naphthalene ring. A slight shift of the peaks to a higher wavenumber is seen as a consequence of the Stark effect. Above 0.96 V, no strong features are noticeable in the spectra, which also agrees

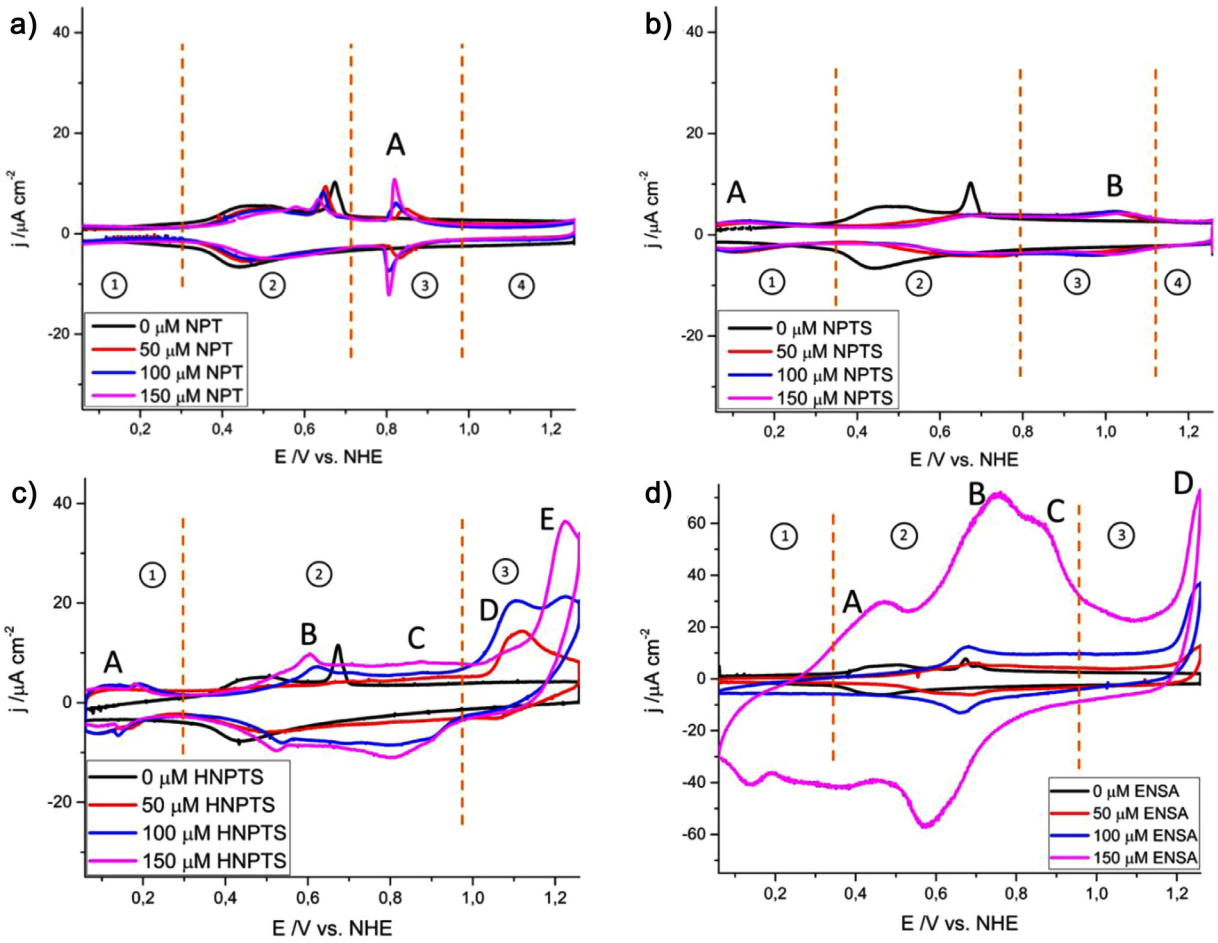

Fig. 5. Cyclic voltammograms of Au (100), 0.1 M H_2SO_4 at different concentrations of (a) NPT (b) NPTS and (c) HNPTS (d) ENSA recorded between 0.06 to 1.26 V DL- region, at 50 mV s^{-1}.

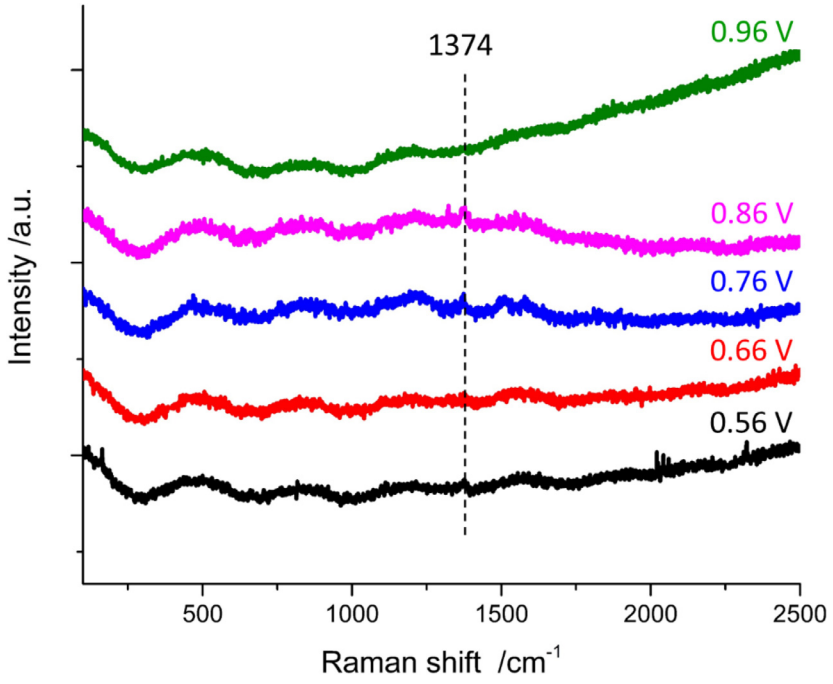

Fig. 6. SER spectrum of 0.2 mM of NPT in 0.1 M H_2SO_4 on polycrystalline gold at different potentials from 0.56 to 0.96 V, see band at 1374 cm^{-1}; The full spectrum recorded between 0.01 to 1.06 V is shown in Fig. S8.

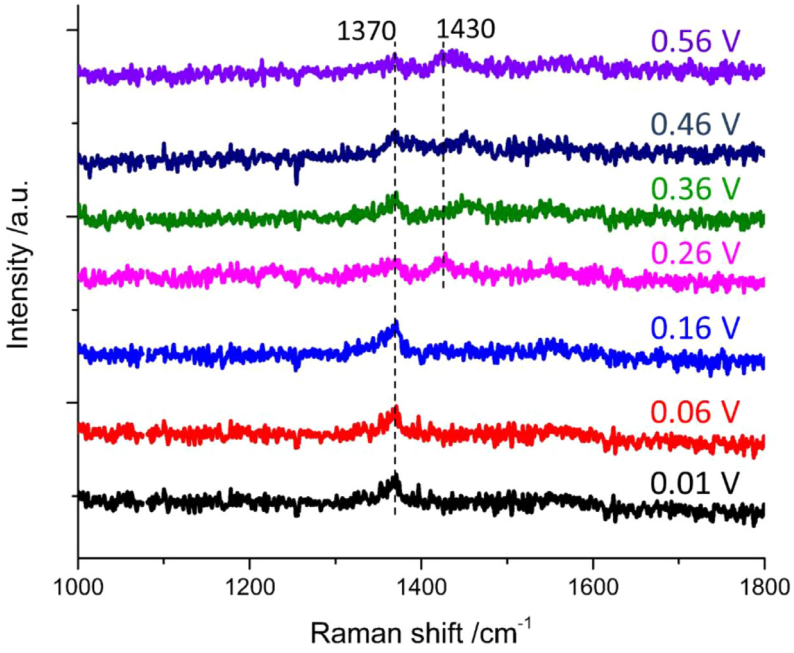

Fig. 7. SER spectrum of 1 mM of NPTS in 0.1 M H_2SO_4 on polycrystalline gold at different potentials from 0.01 to 0.56 V, see bands at 1370 and 1430 cm^{-1}; The full spectrum recorded between 0.01 to 1.06 V is shown in Fig. S9.

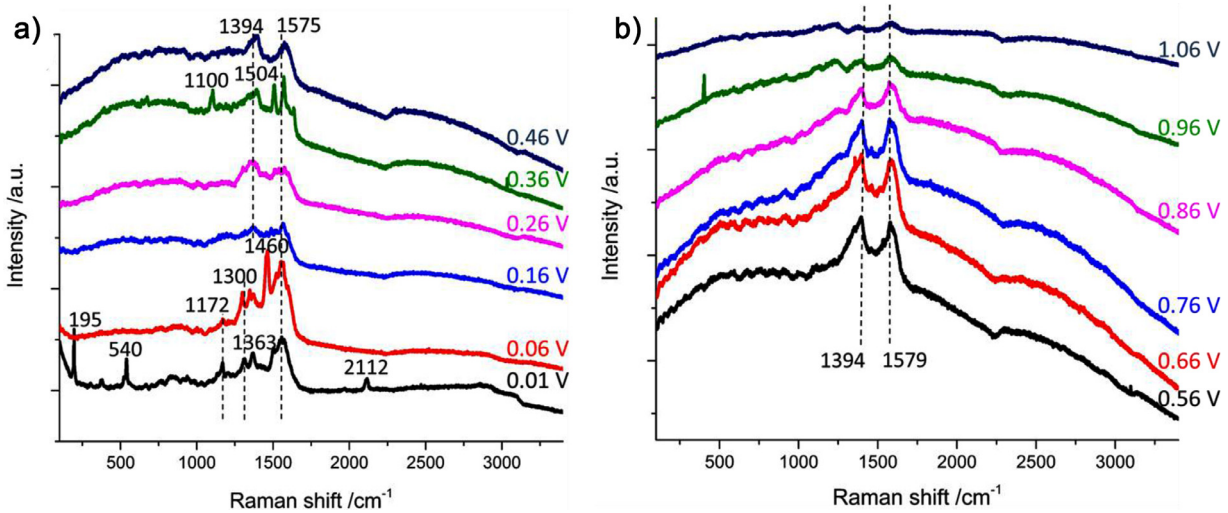

Fig. 8. SER spectra of 1 mM of HNPTS in 0.1 M H_2SO_4 on polycrystalline gold at different potentials: (a) detailed spectra from 0.01 to 0.46 V; (b) detailed spectra from 0.56 to 1.06 V. The full spectra are shown in Fig. S10.

with the abrupt increase in the current due to peaks C, D, E (see Fig 5c).

The above observations suggest that HNPTS does not lie flat on the surface, in contrast to NPT and NPTS. Moreover, it is seen that above 0.96 V it undergoes a complex process that is not sensitive to the electrode surface, which we tentatively ascribe to oxidative polymerization of the naphthol group [40–43].

Fig 9a shows the evolution of the ENSA spectra between 0.01 to 0.26 V. We ascribed band at 1363 cm^{-1} to antisymmetric stretching ν_{as} (-SO_2-) of the sulfonate group [48,49], the band at 1556 cm^{-1} to the symmetric stretching ν_s (C–C) [48] and in-plane bending β(H–C-C) [48–51] of the naphthalene ring and the band at 3150 cm^{-1} to stretching ν (O–H) [48] of the hydroxyl group. We highlight the absence of bands correlated with the ethoxy group at ν_s(C–O-C) [48,49], at ~900 cm^{-1}, ν_s(Aryl-O) [48,49], 1200 – 1300 cm^{-1}. Instead, a band at 2264 cm^{-1} characteristic of C–N stretching is seen, which presumably comes from contamination. Fig 9b shows the spectra between 0.36 to 1.06 V: the spectra exhibit a band at 1326 cm^{-1} ascribed to antisymmetric stretching of sulfonate group ν_{as} (-SO_2-) [48, 49] and 3150 cm^{-1} ascribed to stretching of ν (O–H) [48,49]. A strong increase of the background signal is also observed, implying the formation of a thick film on the electrode surface.

Evolution of SER spectra also suggests that naphthalene ring of ENSA does not lie flat on the electrode surface. Furthermore, the increase in the background upon 0.36 V coincides with the noticeable rise of anodic currents in the cyclic voltammogram, see Fig. 5d. Similarly to HNPTS, oxidative polymerization of naphthol under acidic conditions is suggested to be responsible for this [40–43].

To provide a possible explanation for the difference between the NPT and NPTS films, density functional theory calculations were performed to estimate the lateral interaction of NPT and NPTS molecules (Fig. 10). These calculations show that for NPT the

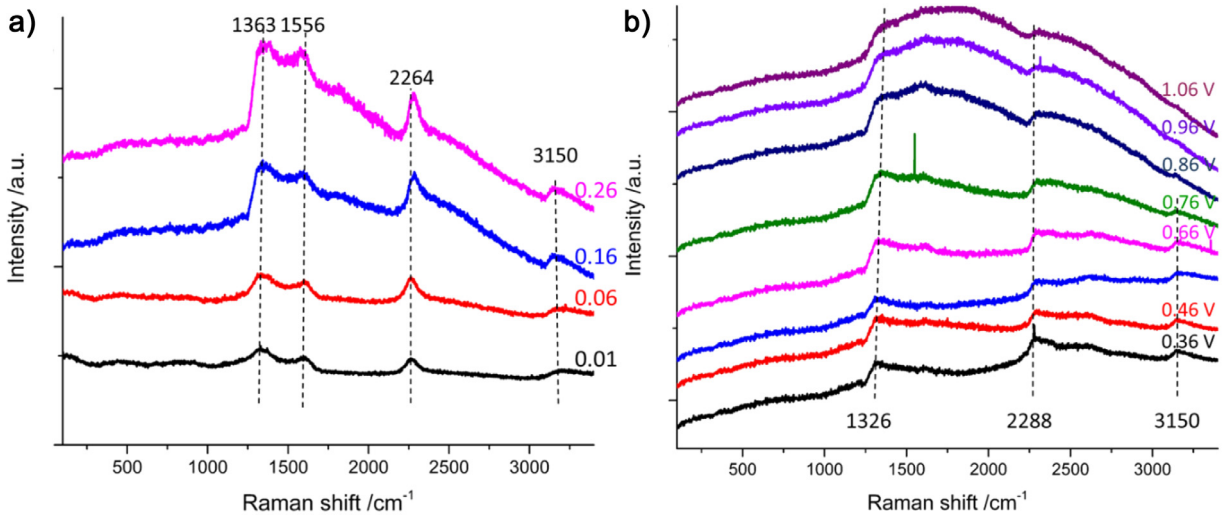

Fig. 9. SER spectrum of 1 mM of ENSA in 0.1 M H_2SO_4 on polycrystalline gold at different potentials (a) detailed spectra from 0.01 to 0.26 V (b) detailed spectra from 0.36 to 1.06 V. The full spectrum is shown in Fig. S11.

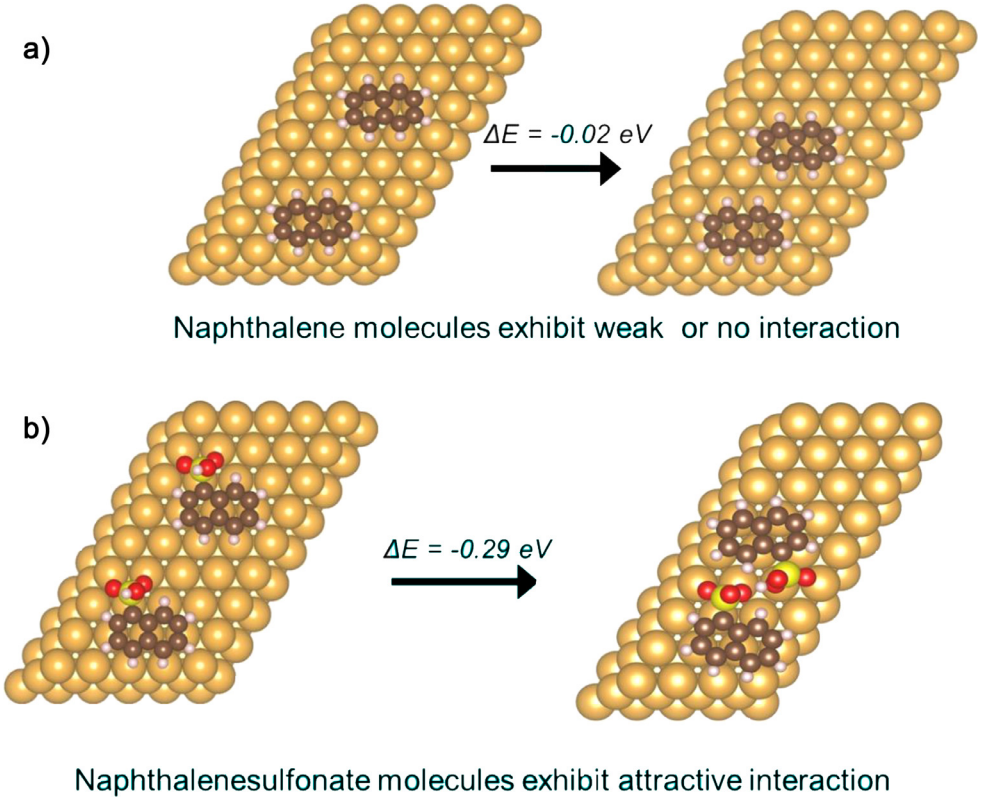

Fig. 10. Difference of lateral interaction energy for (a) NPT and (b) NPTS on Au (111).

interaction between the molecules is weak or negligible, their lateral interaction energy is only −0.02 eV, which was calculated by moving neighboring molecules closer together to neighboring adsorption sites at a constant coverage. On the other hand, for NPTS molecules the lateral interaction energy is −0.29 eV (the negative sign indicates attractive interaction, see Figures S12 and S13 of the supporting information). The difference in lateral interaction energy is caused by the favorable hydrogen bonding formation between NPTS adsorbates; as a consequence, a more compact film is formed between NPTS. This hydrogen bonding could be supported by studies of Ataka and Osawa showing water molecules bridging through hydrogen bonding in sulfate adlayers on Au (111) [53].

These DFT calculations neglect the effect of solvent near the surface and the fraction of protonated sulfonate groups was taken to be 50%. Given that sulfonate is a strong acid, future calculations should consider solvation of the adsorbed molecules and hydrogen bonded pairs. Density functional theory studies were not performed for HNPTS, taking into account the complexity of its behavior due to the possible polymerization [41].

Similar DFT calculations of NPT and NPTS adsorption on metallic tin (α–Sn) were performed, see Figs. 11a and 11b, respectively. A similar behavior in comparison to NPT and NPTS on gold surface is seen. Fig 11a shows that NPT molecules exhibit repulsive lateral interaction, and Fig. 11b shows NPTS molecules ex-

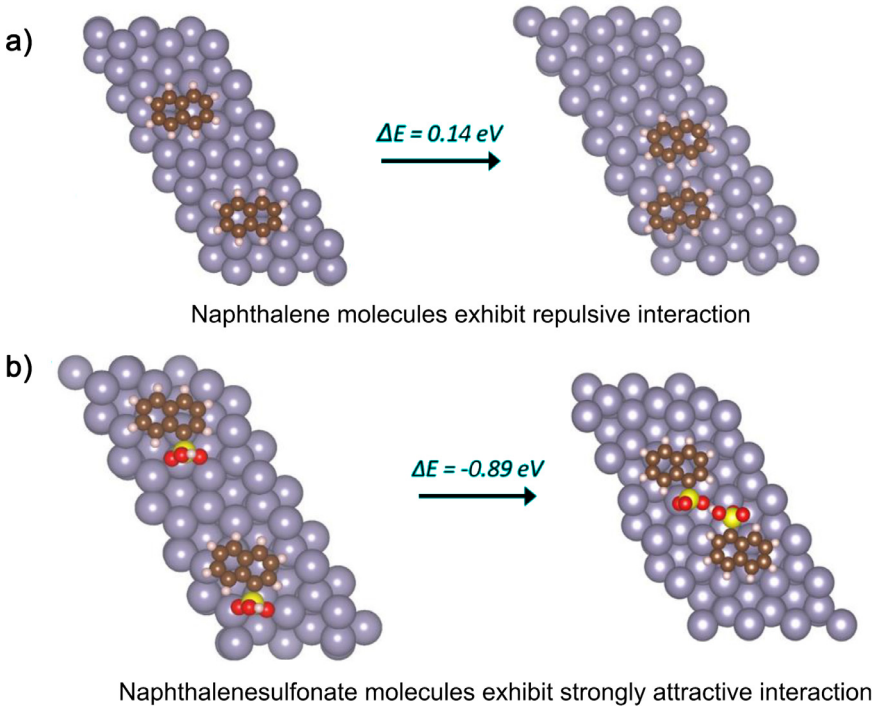

Fig. 11. Difference of lateral interaction energy for (a) NPT and (b) NPTS on Sn (111).

hibit strongly attractive lateral interaction. The observed behavior is agreement with NPT and NPTS binding to gold and tin surfaces mainly through Van der Waals interactions, which are expected to be metal independent. Also, oxidative polymerization is a process which is generally not very sensitive to the nature of the electrode material [40–43]. Therefore, we assume that adsorption structures formed on gold will likely also form on tin. See Figures S13 and S14.

Summarizing, the above electrochemical, spectroscopic and computational results show that NPT and NPTS do not strongly alter the gold CV profile in the sense that the onset potential for the gold (hydr-)oxide formation and HER activity are not affected significantly. However, noticeable changes in the double layer region are present; this region exhibits a decrease in differential capacity, which is characteristic for organic film formation. Studies with single crystal surfaces suggest both NPT and NPTS remain adsorbed over a wide potential range, but that NPTS forms a more compact film than NPT. SER spectroscopy and DFT calculations show that both naphthalene and naphthalenesulfonate bind flat onto the gold surface, and the NPTS exhibits lateral attractive interactions due to hydrogen bonding, which may explain why its film appears to be more compact. On the other hand, HNPTS and ENSA show very different behavior, suggesting oxidative polymerization and polymer film formation.

3.1. Tin electrodeposition on polycrystalline gold in the presence of naphthalene and naphthalenesulfonate

Tin electrodeposition on polycrystalline gold takes place via at least three different deposition mechanisms (irreversible adsorption, underpotential deposition, and overpotential deposition). It has been shown that in the cyclic voltammogram, the deposition process exhibits five distinct peaks: two cathodic peaks associated with tin underpotential and overpotential deposition, and three main anodic peaks, corresponding to the oxidation of the bulk Sn, of the AuSn intermetallic layer, and of the adsorbed Sn(II) to Sn(IV) [54,55]. These processes are summarized by the following equations:

$$C1 : Sn(II)_{ads} + 2e \rightarrow Sn(0)_{UPD} \quad (1)$$

$$C2 : Sn(II)_{sol} + 2e \rightarrow Sn(0)_{OPD} \quad (2)$$

$$A3 : Sn(0)_{OPD} \rightarrow Sn(II)_{sol} + 2e \quad (3)$$

$$A2 : AuSn \rightarrow Au + Sn(II)_{sol} + 2e \quad (4)$$

$$A1 : Sn(II)_{ads} \rightarrow Sn(IV) + 2e \quad (5)$$

Figs. 12a, 13a and 14a show the cyclic voltammograms at a gold rotating disk electrode (RDE) in an extended range of potential (−0.54 to 0.66 V) with and without NPT, NPTS and HNPTS at different concentrations.

It is observed in Fig. 12a that the peak related to stripping of the bulk deposited tin (A3) decreases considerably in the presence of NPT, showing that a smaller amount of tin has been deposited. An increase in the cathodic current at the most negative potentials is also seen, which has been ascribed to the concurrent reaction of hydrogen evolution reaction (HER) on the remaining gold surface [55]. This higher HER current also suggests a decrease in the amount of tin deposited as this will lead to a higher surface area of gold available for HER, in agreement with the previous observation of island formation during tin deposition on gold [56,55]. Furthermore, no changes are seen in the stripping of the alloy AuSn (A2, A2') and in the Sn(II) oxidation process (A1), neither in the current densities nor in the potential of the respective processes.

Since all the cyclic voltammetry measurements were performed at the same scan rate and rotation speed, peak A3 is a good marker to estimate the amount of tin bulk deposited. From the voltammetric information, naphthalene does not seem to affect strongly most of the reactions involved during the deposition and stripping processes, other than it generally seems to slow down the tin reduction.

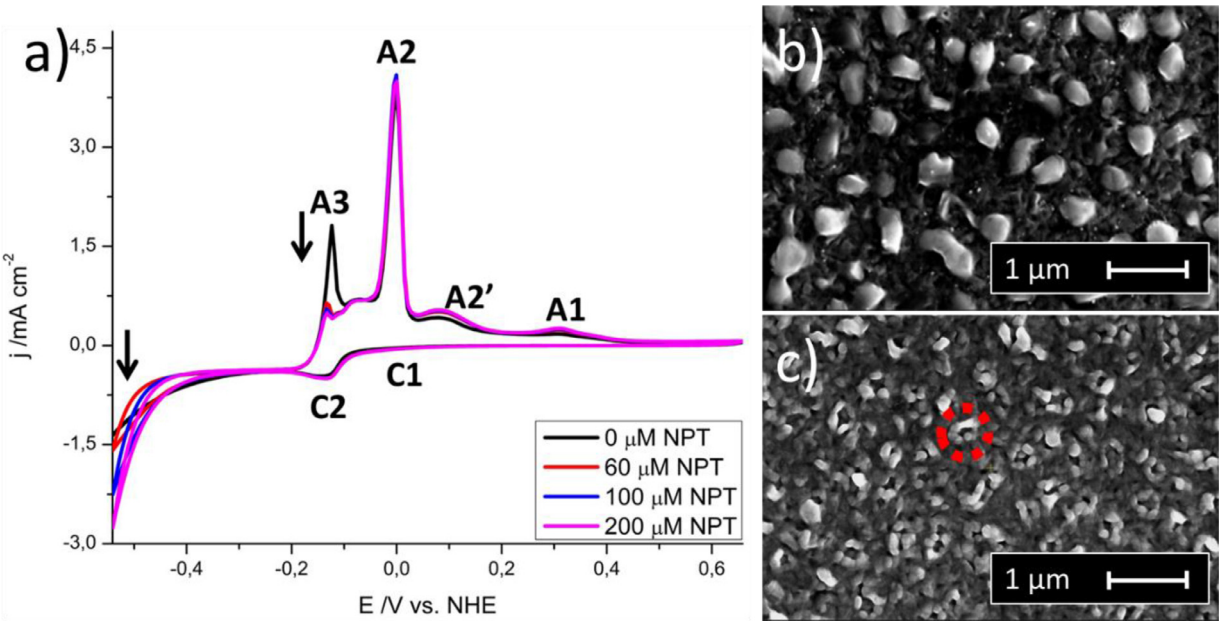

Fig. 12. (a) Cyclic voltammograms of tin electrodeposition on a polycrystalline gold RDE, 0.1 M H_2SO_4 at different concentrations of NPT, recorded between −0.541 to 0.659 V and 30 mV s^{-1} and 1600 rpm. SEM micrographs of tin electrodeposited, on polycrystalline gold; potential was swept from 0.659 to −0.241 V at 30 mV s^{-1} and 1600 rpm, subsequently the potential was held at −0.241 V during 1 min, 0.1 M H_2SO_4, 0.6 mM $SnSO_4$, in the presence of: (b) without *NPT* (c) with 200 μM NPT.

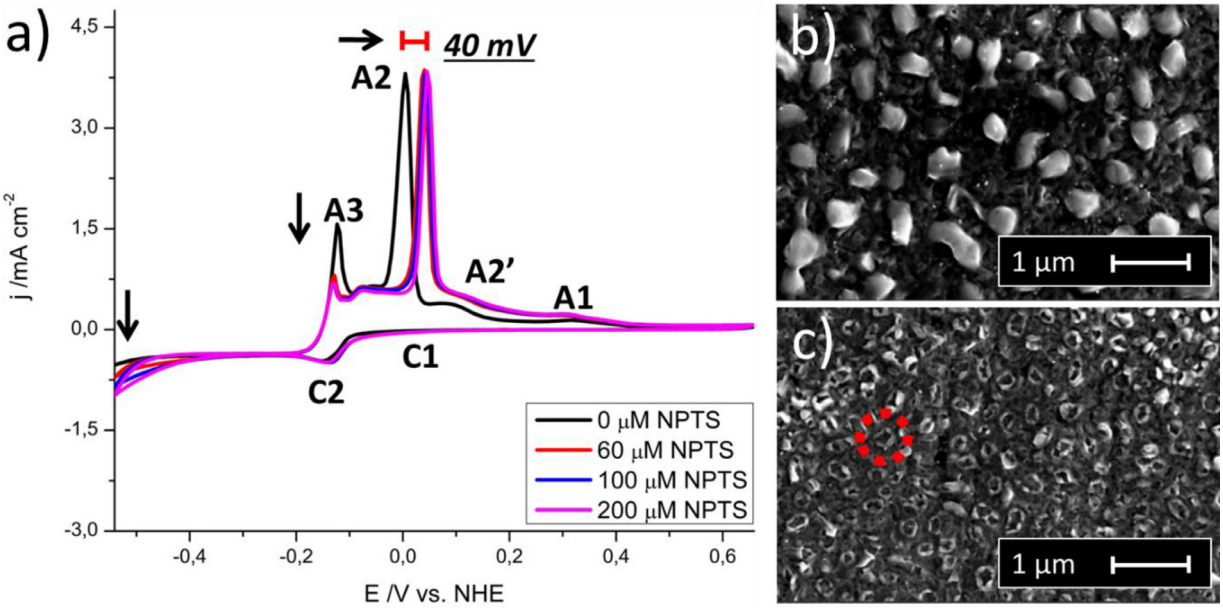

Fig. 13. (a) Cyclic voltammograms of tin electrodeposition on RDE polycrystalline gold, 0.1 M H_2SO_4 at different concentrations of NPTS, recorded between −0.541 to 0.659 V and 30 mV s^{-1} and 1600 rpm. SEM micrographs of tin electrodeposited on polycrystalline gold, potential was swept from 0.659 to −0.241 V at 30 mV s^{-1} and 1600 rpm, subsequently potential was held at −0.241 V during 1 min, 0.1 M H_2SO_4, 0.6 mM $SnSO_4$, in the presence of: (b) without NPTS (c) with 200 μM NPTS.

Figs. 12b and 12c show the SEM images of the morphology of the tin deposit in the absence and presence of naphthalene, respectively. The deposit in the absence of naphthalene exhibits a low density and large 3D nuclei, with features sizes between 300 – 900 nm. On the other hand, in the presence of naphthalene, the deposit exhibits a higher number of nuclei and smaller feature size (<100 nm) that appear coalesced. Moreover, the deposit seems to be organized in a circular arrangement (see Fig 12c – doted red line). The number of tin deposited monolayers shows almost not differences in the number of equivalent tin layers from $\theta_{Sn(0\,\mu M\,NPT)} = 50\,ML$ to $\theta_{Sn(0\,\mu M\,NPT)} = 49\,ML$. These observations suggests that NPT acts to slow down only the tin bulk electrodeposition process, yielding smaller features which are presumably primarily AuSn alloy particles.

Fig. 13a shows the effect of naphthalenesulfonate on tin electrodeposition process. In accordance with the effect of NPT, NPTS also gives rise to a decrease in the peak A3, related to the oxidation of bulk deposited tin, and an increase of the HER current on gold at the most negative potentials. SEM micrographs also show a decrease of the feature size with NPTS and production of circular shapes, the tin deposit also exhibits a higher number of nuclei (Fig. 13c), very similar to NPT. Furthermore, a slight (though perhaps not very significant) increase in the equivalent number of tin layers from $\theta_{Sn\,(0\,\mu M\,NPTS)} = 50\,ML$ to $\theta_{Sn\,(200\,\mu M\,NPTS)} = 54\,ML$ and a

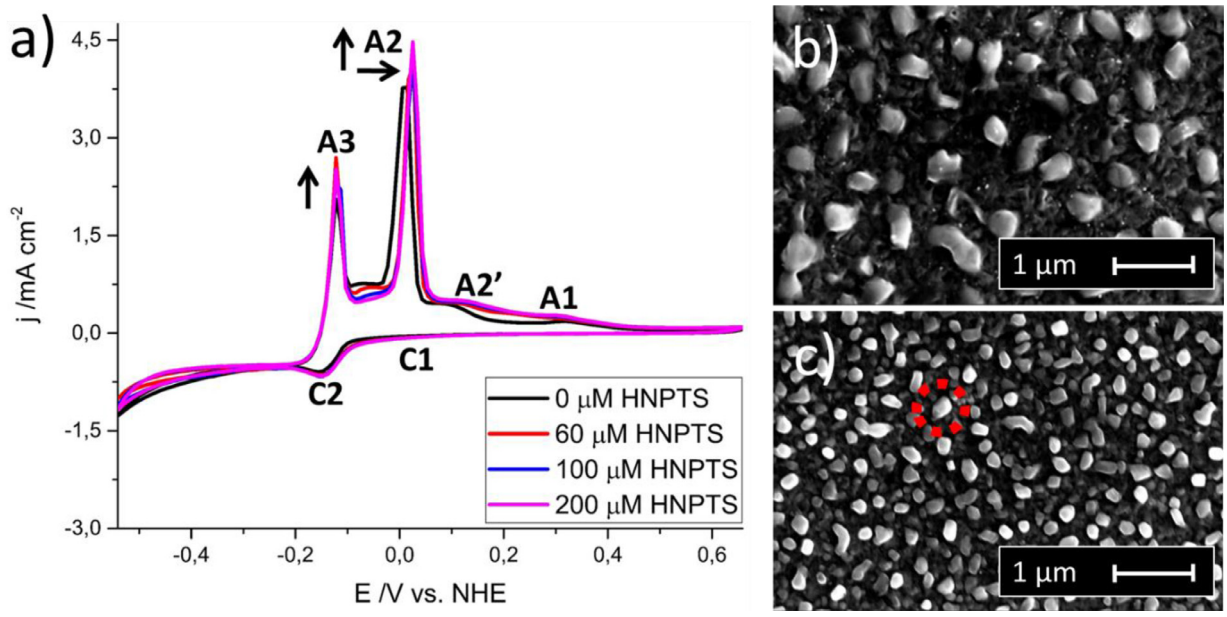

Fig. 14. (a) Cyclic voltammograms of tin electrodeposition on a polycrystalline gold RDE, 0.1 M H_2SO_4 at different concentrations of HNPTS, recorded between −0.541 to 0.659 V and 30 mV s^{-1} and 1600 rpm. SEM micrographs of tin electrodeposited, on polycrystalline gold; potential was swept from 0.659 to −0.241 V at 30 mV s^{-1} and 1600 rpm, subsequently potential was held at −0,241 V during 1 min, 0.1 M H_2SO_4 0.6 mM $SnSO_4$, in the presence of: (b) without HNPTS (c) with 200 μM HNPTS.

more condensed structure of the deposit are observed. Additionally, a shift in the peak A2, attributed to stripping of the Au-Sn alloys. Voltammograms at different scan rates show that this shift is not kinetic in nature (see Fig S15 in the Supporting Information).

Fig. 14a shows the cyclic voltammogram of tin electrodeposition in the presence of HNPTS. Unlike NPT and NPTS, HNPTS exhibits an increase in both peak A3 and A2, related to the oxidation of bulk electrodeposited tin and tin-gold alloys, resp.. A small increase of the number of equivalent tin layers from $\theta_{Sn\,(0\,\mu M\,HNPTS)} = 50\,ML$ to $\theta_{Sn\,(200\,\mu MHNPTS)} = 55\,ML$ is observed, as well as of the intensities of the A2 and A3 peaks, suggest that a higher amount of tin bulk and AuSn alloy have been deposited. SEM micrographs in the absence and presence of HNPTS also show remarkable differences; the tin deposit exhibits a higher 3D nuclei density, with a smaller feature size (about 100 nm). Unlike tin deposits in the presence of NPT and NPTS, the features do not appear coalesced. The voltammogram also shows an increase in the HER and a shift in the peak A2, which is again not kinetic in nature.

We ascribe the shift in the potential of peak A2 for NTPS and HNPTS to the incorporation of some form of sulfur in the AuSn deposit. The incorporation of sulfur in nickel deposits due to reduction of allylsulfonates has been observed previously by Gotthard and Trivich [57], who proposed it to happen via an early desulphonation. Later, Kendrick [58] also mentioned the sulfur incorporation during nickel electrodeposition caused by reduction of naphthalene derivatives and proposed two mechanisms: via mercaptan formation and via an early desulphonation. Brook and Crossley also showed the presence of sulfur in nickel deposits and claimed that the process happens via an early desulphonation, with a thiosulfate as intermediate [59]. These reactions are described by the following equations:

$$R - SO_3H + 2e \rightarrow R - H + {SO_3}^{2-} \quad (6)$$

$$2{SO_3}^{2-} + 6H_3O^+ + 4e \rightarrow {S_2O_3}^{2-} + 9H_2O \quad (7)$$

$${S_2O_3}^{2-} + 2Ni + 6H_3O^+ + 4e \rightarrow 2NiS + 9H_2O \quad (8)$$

In the case of nickel electroplating in the presence of naphthalenesulfonic acid, Brook and Crossley showed the presence of naphthalene via extraction with amyl acetate and subsequent identification via UV spectroscopy and chromatography. However, the presence of thiosulfate as an intermediate was not corroborated.

Fig. 15 shows cyclic voltammograms of tin electrodeposition in the absence and presence of naphthalene and with different concentrations of sodium thiosulfate. Voltammograms in the absence of thiosulfate (black and red) exhibit the behavior of the tin deposition in the absence and presence of naphthalene. When thiosulfate is added in the electrolyte, a shift in the A2 peak (ca. 40 mV) is seen which perfectly agrees with the shift observed in the presence of NPTS and HNPTS. This observation agrees with the assertion of Brook and Crossley that thiosulfate may act as an intermediate in the sulfur incorporation in the metal deposit, though we do not claim it to be the intermediate for NPTS, HNPTS and ENSA. More importantly, it shows that the peak shift observed in the presence of NPTS and HNPTS is most likely due to some form of sulfur incorporation in the deposit.

3.2. Tin electrodeposition on polycrystalline gold in the presence of ethoxylated napthalenesulfonic acid (ENSA - 6)

Fig. 16 shows the cyclic voltammetry of tin electrodeposition in the absence and presence of ENSA–6. Compared to NPT, NPTS and HNPTS, in the presence of ENSA show there is a much stronger inhibition effect on tin bulk deposition, as evidenced by the decrease in the peak A3. Fig. 16a also shows a shift in the potential of the peak A2 ascribed to sulfur incorporation in the AuSn alloy.

The equivalent number of tin layers was calculated for the deposit shown in the SEM image, showing a decrease from $\theta_{Sn\,(0\,\mu M\,ENSA)} = 50\,ML$ to $\theta_{Sn\,(200\,\mu M\,ENSA)} = 29\,ML$. The scanning electron micrograph shows almost no tin features on the substrate, apart perhaps from a few tin features along the substrate defects. Fig. 17 shows the relative sulfur and tin abundance on the substrate for all the naphthalene-based additives. Tin deposited in the presence of NPTS, HNPTS and ENSA exhibit sulfur, although the values are very dispersed and hardly above the noise, so that further spectroscopic studies are required to unveil the nature and quantity of the sulfur compound(s) present in the deposit. Moreover, Fig. 17 also shows that ENSA exhibits the lowest amount of

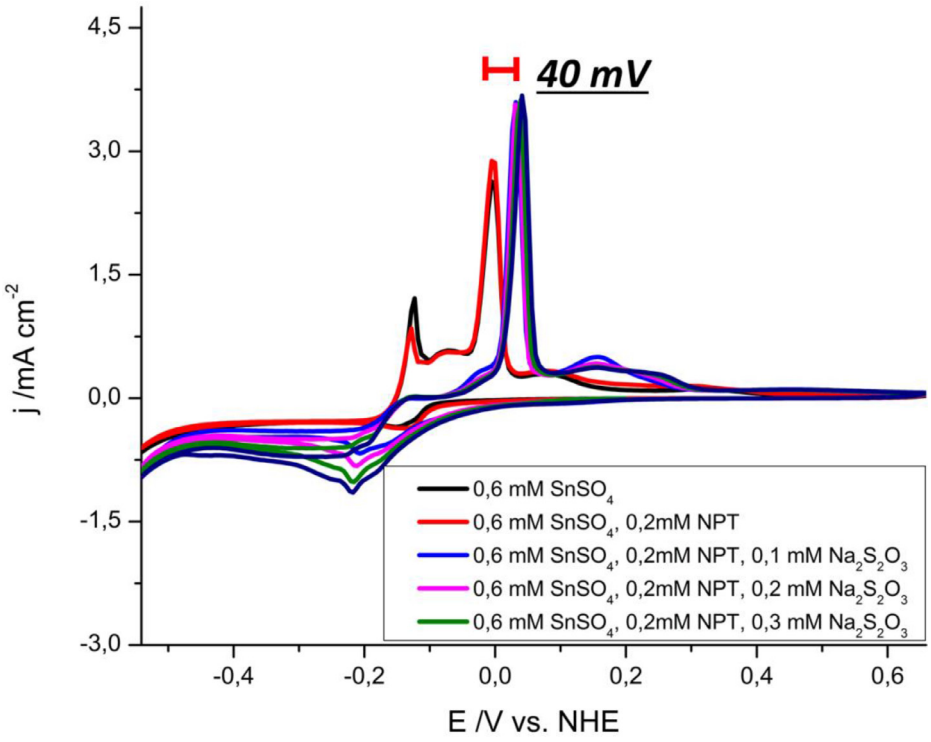

Fig. 15. Cyclic voltammogram of tin electrodeposition on polycrystalline gold, 0.1 M H_2SO_4, 0.6 mM $SnSO_4$, 0.2 mM *NPT*, 30 mVs^{-1} and 1600 rpm.

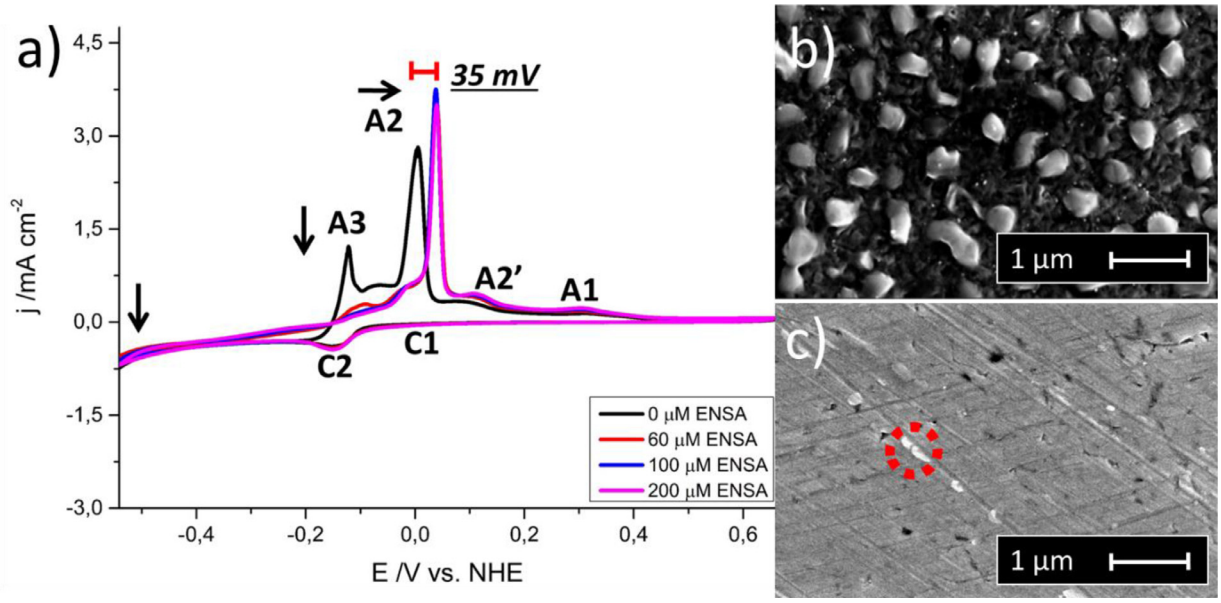

Fig. 16. (a) Cyclic voltammograms of tin electrodeposition on RDE polycrystalline gold, 0.1 M H_2SO_4, 0.6 mM $SnSO_4$ at different concentrations of ENSA, recorded between −0.541 to 0.659 V at 30 mV s^{-1} and 1600 rpm. SEM micrographs of tin electrodeposited on polycrystalline gold, potential was swept from 0.659 to −0.241 V at 30 mV s^{-1} and 1600 rpm, subsequently potential was held at −0.241 V during 1 min, (b) without *ENSA* (c) with 200 µM *ENSA*.

tin. This agrees with the SEM image which basically shows an essentially featureless AuSn alloy surface. Previous studies of the effect of ENSA on tin electrodeposition on different substrates have ascribed the inhibition of the tin deposition to a decrease of the rate of electron transfer [19], and to Sn(II) mass transport limitations to the substrate surface caused by a compact stable layer of ENSA molecules on the surface [20]. Our work shows that ENSA does not remain stable on the Au surface, instead it may undergo an oxidative polymerization process. Furthermore, for Sn electrodeposition on gold, ENSA mainly seems to have an effect on tin bulk deposition process, and it shows little effect on the AuSn alloying process; except from sulfur incorporation into the alloy and a slight increase in the charge associated to the dealloying peak from 5.5 (0 mM ENSA) to 5.7 mC/cm^2 (0.2 mM ENSA), similar values of the charge for AuSn dealloying process were previously reported by Petersson et al. [54] . Results show that ENSA strongly inhibits the 3D growth of the tin features, but promotes the Au-Sn alloying process. Moreover, ENSA exhibits almost no effect on the early stages of the tin deposition on gold, unlike previous studies [20] that suggested that ENSA molecules also have a

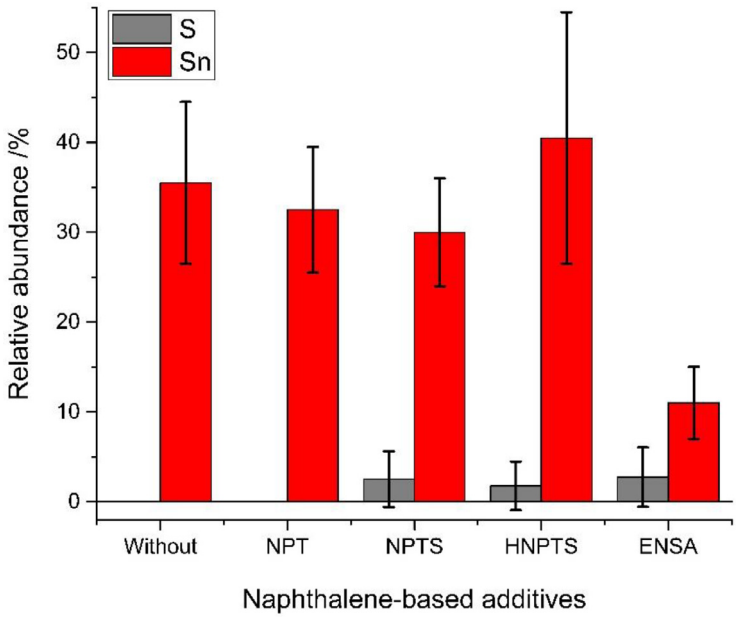

Fig. 17. Comparison of the tin and sulfur relative abundance for each additive from the EDS measurements. Percentage was calculated from the average of the relative ratio of tin in a line scan measurement of about ~0.5 µm length, over the tin features.

strong influence on early stages of the tin deposition on iron electrodes.

Additionally, the above results show that tin deposits grown in the absence and presence of additives all show a very similar AuSn alloy stripping peak (apart from sulfur-related shift). This suggests that the alloying itself is hardly influenced by the presence of additives, and therefore more likely related to the very early stages of tin deposition (such as UPD), and not much related to the growth of bulk tin features.

Previous in situ STM studies by Mao et al. [56,60] have demonstrated the complex nature of Sn UPD on Au single crystal electrodes, with the UPD intimately linked to the surface alloying process. They showed that underpotential deposition of Sn on Au presents strikingly different features from usual UPD processes, such as distorted and size confined clustering, preferential nucleation, anisotropic growth, and the formation of an disordered adlayer on Au (111) surfaces [56]. Mao et al. show a strong correlation between surface alloying and the unusual UPD, in the sense that Sn forms clusters of about 2 nm size, which remain stable over time, and depending on the electrode potential and substrate surface structure, Sn diffuses into the gold lattice, as a result of which SnAu alloying would take place. Tin underpotential deposition and alloy formation also exhibit a slow kinetics [56].

Given the slow kinetics of the underpotential deposition and the associated alloy formation, the relatively small effect that ENSA but also NPT, NPTS and HNPTS exhibit on the alloying process seems reasonable. Our measurements suggest that a certain amount of tin adatoms on the gold surface go through UPD and subsequent surface alloying without being affected by the presence of naphthalene derivatives on the surface. The amount of alloying would only be affected by changes in the gold interdiffusion barrier, which is apparently not affected by the additive. In contrast, the kinetics of tin overpotential process is fast and as a consequence, Sn OPD deposition is affected by additive adsorption, due to a kinetic effect.

Conclusions

In this study, we have investigated the effect of naphthalene derivatives, NPT, NPTS, HNPTS, and ENSA, on the tin electrodeposition process on a gold electrode. From experiments and density functional theory calculations, we conclude the formation of films of NPT, NPTS, HNPTS and ENSA. NPT and NPTS lie flat on the gold surface. NPTS forms a denser film due to attractive interactions via hydrogen bonding between the adsorbed molecules, and HNPTS and ENSA forms surface films as a result of oxidative polymerization. Tin electrodeposition is strongly affected by the presence of the NPT, NPTS, HNPTS, and ENSA films. Tin bulk electrodeposition is inhibited in the presence of NPT and NPTS, but promoted in the presence of HNPTS. Tin deposits grown in the presence of NPT and NTPS seem to have the same morphology, but tin deposit grown in the presence of HNPTS exhibits markedly smaller features. Sulfonated additives lead to some form of sulfur incorporation in the SnAu alloys as a consequence of reductive desulphonation and subsequent sulfonate reduction; thiosulfate was identified as a possible intermediate in this reaction.

Ethoxylated napthalenesulfonic acid (ENSA), a commonly used additive in the tin electroplating industry, exhibits a similar behavior to NPT and NPTS during the tin deposition process in terms of the measured voltammetry: a suppression of the bulk Sn electrodeposition, but essentially no effect on the AuSn alloy formation, besides sulfur incorporation. Nonetheless, SEM shows that ENSA severely inhibits the tin bulk deposition to the extent that the surface shows no notable features in the SEM images. Finally, the lack of a strong effect of naphthalene derivatives and ENSA on the SnAu alloying process is ascribed to the slow nature of Sn UPD on gold and SnAu alloying process.

Declaration of Competing Interest

None

Credit authorship contribution statement

D. Aranzales: Conceptualization, Methodology, Investigation, Writing - original draft. **I. Briliani:** Methodology, Investigation. **I.T. McCrum:** Methodology, Investigation. **J.H.O.J. Wijenberg:** Conceptualization, Writing - review & editing, Supervision, Funding acquisition. **A.C.A. de Vooys:** Writing - review & editing. **M.T.M. Koper:**

Conceptualization, Writing - review & editing, Supervision, Funding acquisition.

Acknowledgment

This research was sponsored by Tata Steel Nederland Technology B.V. through the Materials Innovation Institute M2i and the Technology Foundation TTW, which is the applied science division of the Netherlands Organization for Scientific Research (NWO) and the Technology Programme the Ministry of Economic Affairs of the Netherlands.

Supplementary materials

Supplementary material associated with this article can be found, in the online version, at doi:10.1016/j.electacta.2020.137606.

References

[1] M. Paunovic, M. Schlesinger, Fundamentals of Electrochemical Deposition Second Edition, Sceond., A JOHN WILEY & SONS, United States of America, 2006.
[2] T.C. Franklin, Some mechanisms of action of additives in electrodeposition processes, Surf. Coatings Technol. 30 (4) (1987) 415–428.
[3] L. Oniciu, L. Muresan, Some fundamental aspects of levelling and brightening in metal electrodeposition, J. Appl. Electrochem. 21 (7) (1991) 565–574.
[4] C.M. Whelan, M.R. Smyth, C.J. Barnes, The influence of heterocyclic thiols on the electrodeposition of Cu on Au(111), J. Electroanal. Chem. 441 (1–2) (1998) 109–129.
[5] M. Petri, D.M. Kolb, U. Memmert, H. Meyer, Adsorption of PEG on Au(111) single-crystal electrodes and its influence on copper deposition, J. Electrochem. Soc. 151 (12) (2004) C793.
[6] Y. Yanson, J.W.M. Frenken, M.J. Rost, A general model of metal underpotential deposition in the presence of thiol-based additives based on an in situ STM study, Phys. Chem. Chem. Phys. 13 (35) (2011) 16095–16103.
[7] M.H. Hoizle, C.W. Apsel, T. Will, D.M. Kolb, Copper deposition onto Au(l 11) in the presence of thiourea, J. Electrochem. Soc. 142 (11) (1995) 3741–3749.
[8] Z. Shi, S. Wu, J. Lipkowski, Investigations of Cl – adsorption at the Au(111) electrode in the presence of underpotentially deposited copper atoms, J. Electroanal. Chem. 384 (1–2) (1995) 171–177.
[9] S. Wu, Z. Shi, J. Lipkowski, A.P. Hitchcock, T. Tyliszczak, Early stages of copper electrocrystallization: electrochemical and in situ x-ray absorption fine structure studies of coadsorption of copper and chloride at the Au(111) electrode surface, J. Phys. Chem. B 101 (49) (1997) 10310–10322.
[10] E. Herrero, L.J. Buller, H.D. Abruña, Underpotential deposition at single crystal surfaces of Au, Pt, Ag and other materials, Chem. Rev. 101 (7) (2001) 1897–1930.
[11] O.M. Magnussen, Atomic structure of ordered copper adlayers on single-crystalline gold electrodes, J. Vac. Sci. Technol. B Microelectron. Nanom. Struct. 9 (2) (1991) 969.
[12] D.M. Kolb, Reconstruction phenomena at metal-electrolyte interfaces, Prog. Surf. Sci. 51 (2) (1996) 109–173.
[13] F.C. Walsh, C.T.J. Low, A review of developments in the electrodeposition of Tin, Surf. Coatings Technol. 288 (2016) 79–94.
[14] R. Sekar, C. Eagammai, S. Jayakrishnan, Effect of additives on electrodeposition of tin and its structural and corrosion behaviour, J. Appl. Electrochem. 40 (1) (2010) 49–57.
[15] Y. Nakamura, N. Kaneko, H. Nezu, Surface morphology and crystal orientation of electrodeposited tin from acid stannous sulphate solutions containing various additives, J. Appl. Electrochem. 24 (6) (1994) 569–574.
[16] N. Kaneko, N. Shinohara, H. Nezu, Effects of aromatic carbonyl compounds on the surface morphology and crystal orientation of electrodeposited tin from acid stannous sulfate solutions, Electrochim. Acta 37 (13) (1992) 2403–2409.
[17] N.M. Martyak, R. Seefeldt, Additive-effects during plating in acid tin methanesulfonate electrolytes, Electrochim. Acta 49 (25) (2004) 4303–4311.
[18] F.J. Barry, V.J. Cunnane, Synergistic effects of organic additives on the discharge, nucleation and growth mechanisms of tin at polycrystalline copper electrodes, J. Electroanal. Chem. 537 (1–2) (2002) 151–163.
[19] C.J. Van Velzen, M. Sluyters-Rehbach, J.H. Sluysters, The electrochemical reduction of Sn (II) at the dropping mercury electrode from aqueous 1M sulfuric acid and from 0.3M phenolsulphonic acid and its inhibition by ENSA -6, Electrochim. Acta 32 (5) (1987) 815–821.
[20] J.-Y. Lee, J.-W. Kim, B.-Y. Chang, H. Tae Kim, S.-M. Park, Effects of ethoxylated α-naphtholsulfonic acid on tin electroplating at iron electrodes, J. Electrochem. Soc. 151 (5) (2004) C333.
[21] R. Stuart Tobias, Studies of the hydrolysis of metal ions: the hydrolysis of the tin (II) Ion, Sn(II), Acta Chem. Scand. 12 (1958) 198–223.
[22] M. Pettine, F.J. Millero, G. Macchi, Hydrolysis of tin(II) in aqueous solutions, Anal. Chem. 53 (7) (1981) 1039–1043.
[23] R.M. Cigala, F. Crea, C. De Stefano, G. Lando, D. Milea, S. Sammartano, The inorganic speciation of tin(II) in aqueous solution, Geochim. Cosmochim. Acta 87 (2012) 1–20.
[24] B. Lothenbach, M. Ochs, H. Wanner, M. Yui, Thermodynamic data for the speciation and solubility of Pd, Pb, Sn, Sb, Nb and Bi in aqueous solution, Japan Nucl. Cycle Dev. Inst. (2004) 1–356.
[25] S. Trasatti, O.A. Petrii, Real surface area measurements, J. Electroanal. Chem. 327 (1–2) (1992) 353–376.
[26] G. Kresse, J. Furthmüller, Efficient iterative schemes for ab initio total-energy calculations using a plane-wave basis set, Phys. Rev. B 54 (16) (1996) 11169–11186.
[27] G. Kresse, J. Furthmüller, Efficiency of ab-initio total energy calculations for metals and semiconductors using a plane-wave basis set, Comput. Mater. Sci. (1996).
[28] G. Kresse, J. Hafner, Ab initio molecular dynamics for liquid metals, Phys. Rev. B 47 (1) (1993) 558–561.
[29] P.E. Blöchl, Projector augmented-wave method, Phys. Rev. B 50 (24) (1994) 17953–17979.
[30] G. Kresse, D. Joubert, From ultrasoft pseudopotentials to the projector augmented-wave method, Phys. Rev. B 59 (3) (1999) 1758–1775.
[31] J.P. Perdew, K. Burke, M Ernzerhof, Generalized gradient approximation made simple, Phys. Rev. Lett. 77 (18) (1996) 3865–3868.
[32] J.P. Perdew, K. Burke, M. Ernzerhof, Perdew, Burke, and Ernzerhof reply, Phys. Rev. Lett. 80 (4) (1998) 891.
[33] R.W.G. Wyckoff, Crystal Structures, Interscience, Ed., Wiley, New York, 1963 Vol. 1.
[34] R. Tran, Z. Xu, B. Radhakrishnan, D. Winston, W. Sun, K.A. Persson, S.P. Ong, Surface energies of elemental crystals, Sci. Data 3 (1) (2016) 160080.
[35] S. Grimme, J. Antony, S. Ehrlich, H. Krieg, A consistent and accurate ab initio parametrization of density functional dispersion correction (DFT-D) for the 94 elements H-Pu, J. Chem. Phys. 132 (15) (2010) 154104.
[36] S. Grimme, S. Ehrlich, L. Goerigk, Effect of the damping function in dispersion corrected density functional theory, J. Comput. Chem. 32 (7) (2011) 1456–1465.
[37] L.-J. Wan, K. Itaya, In situ scanning tunneling microscopy of benzene, naphthalene, and anthracene adsorbed on Cu(111) in solution, Langmuir 13 (26) (1997) 7173–7179.
[38] G. Jarzabek, Z. Borkowska, Adsorption of dimethylsulphoxide on the polycrystalline gold electrode from aqueous solutions, J. Electroanal. Chem. 248 (2) (1988) 399–410.
[39] U. Retter, H. Lohse, On the temperature dependence of the two-dimensional condensation of adenosine at the mercury/electrolyte interface, J. Electroanal. Chem. Interfacial Electrochem. 134 (2) (1982) 243–250.
[40] M.C. Pham, J. Moslih, C. Barbero, O. Haas, Influence of the cation size on the charge compensation process in poly(1-naphthol) coated electrodes. multiple internal reflection FTIR spectroscopy (MIRFTIRS) and probe beam deflection (PBD) study, J. Electroanal. Chem. 316 (1–2) (1991) 143–154.
[41] D. Laser, M. Ariel, Electro-optical study of the oxidative adsorption of 1-naphthol on platinum and gold film electrodes, Electroanal. Chem. Interfacial Electrochem. 35 (1972) 405–414.
[42] M.G.D.W. Kirk, The electrochemical oxidation of aqueous phenol at a glassy carbon electrode, Can. J. Chem. Eng. 68 (1981) (1990) 997–1003.
[43] M. Panizza, G. Cerisola, Influence of anode material on the electrochemical oxidation of 2-naphthol: part 1. Cyclic voltammetry and potential step experiments, Electrochim. Acta 48 (23) (2003) 3491–3497.
[44] M. Kleinert, A. Cuesta, L.A. Kibler, D.M. Kolb, In situ observation of an ordered sulfate adlayer on Au (100) electrodes, Surf. Sci. 430 (1) (1999) 521–526.
[45] C.C. Busy, J.A. Creighton, Efficient gold and silver electrodes for surface enhanced raman spectral studies of electrochemical systems: the behaviour of pridine and naphthalene adsorbed on roughened gold electrodes, J. Electroanal. Chem 140 (1982) 379–390.
[46] H. Dahms, M. Green, The adsorption of aromatic hydrocarbons at the gold electrolyte interface, J. Electrochem. Soc. 110 (10) (1963) 1075–1080.
[47] L. Wan, K. Itaya, In situ scanning tunneling microscopy of benzene, naphthalene, and anthracene adsorbed on Cu(111) in solution, Langmuir 13 (26) (1997) 7173–7179.
[48] D. Lin-Vien, N.B. Colthup, W.G. Fateley, J.G. Grasselli, The Handbook of Infrared and Raman Characteristic Frequencies of Organic Molecules, Academic Press, 1991.
[49] P Larkin, IR and Raman spectra-structure correlations, Infrared Raman Spectrosc. (2011) 73–115.
[50] S. Sebastian, S. Sylvestre, N. Sundaraganesan, M. Amalanathan, S. Ayyapan, K. Oudayakumar, B. Karthikeyan, Vibrational spectra, molecular structure, natural bond orbital, first order hyperpolarizability, TD-DFT and thermodynamic analysis of 4-amino-3-hydroxy-1- naphthalenesulfonic acid by DFT approach, Spectrochim. Acta - Part A, 107 (2013) 167–178.
[51] H. Sellers, P. Pulay, J.E. Boggs, Theoretical prediction of vibrational spectra. 2. Force field, spectroscopically refined geometry, and reassignment of the vibrational spectrum of naphthalene1, J. Am. Chem. Soc. 107 (23) (1985) 6487–6494.
[52] H.I.S. Nogueira, S.M.O. Quintal, Surface-enhanced Raman scattering (SERS) studies on 1,1′-Bi-2-naphthol, Spectrochim. Acta - Part A. 56 (5) (2000) 959–964.
[53] K. Ataka, M. Osawa, In situ infrared study of water–sulfate coadsorption on gold(111) in sulfuric acid solutions, Langmuir 14 (4) (1998) 951–959.
[54] I. Petersson, E. Ahlberg, Kinetics of the electrodeposition of Pb-Sn alloys: part II. At polycrystalline gold electrodes, J. Electroanal. Chem. 485 (2000) 178–187.
[55] D. Aranzales, J.H.O.J. Wijenberg, M.T.M. Koper, Voltammetric study of tin electrodeposition on polycrystalline gold from sulfuric and methanesulfonic acid, J. Electrochem. Soc. 166 (8) (2019) D283–D289.

[56] B.W. Mao, J. Tang, R. Randler, Clustering and anisotropy in monolayer formation under potential control: Sn on Au(111), Langmuir 18 (14) (2002) 5329–5332.
[57] H. Gotthard, D. Trivich, Studien zur elektrolytischen reduktion von natrium-allylsulfonat an nickelkathoden, Electrochim. Acta 7 (3) (1962) 369–383.
[58] R.J. Kendrick, The effects of some aromatic sulphonic acids on the stress, structure, and composition of electrodeposited nickel, Trans. IMF 40 (1) (1963) 19–27.
[59] P.A. Brook, J.A. Crossley, The reduction of some naphthalene derivatives during the electro-deposition of nickel, Electrochim. Acta 11 (9) (1966) 1189–1196.
[60] J.W. Yan, J. Tang, Y.Y. Yang, J.M. Wu, Z.X. Xie, S.G. Sun, B.W. Mao, In situ STM studies on underpotential deposition of Sn on Au(100), Surf. Interface Anal. 32 (1) (2001) 49–52.